Journal of The Electrochemical Society, **160** (11) A2033-A2045 (2013)
0013-4651/2013/160(11)/A2033/13/$31.00 © The Electrochemical Society

Analytical Electrochemical Impedance Modeling of Li-Air Batteries under D.C. Discharge

M. Mehta,[a,b] G. Mixon,[a] J .P. Zheng,[a,b,c,*] and P. Andrei[a,b,z]

[a]*Department of Electrical and Computer Engineering, Florida A&M University and Florida State University, Tallahassee, Florida 32310, USA*
[b]*Aeropropulsion, Mechatronics, and Energy, Florida State University, Tallahassee, Florida 32310, USA*
[c]*Center for Advanced Power Systems, Florida State University, Tallahassee, Florida 32310, USA*

An analytical impedance model and a small-signal equivalent circuit are derived for the impedance spectra of Li-air batteries with porous cathodes. The model takes into consideration the effects of the oxygen diffusion, double layer, and faradaic processes in the cathode and can be applied to Li-air batteries with organic and aqueous electrolytes operating under d.c. discharge. It is shown that the cathode of Li-air batteries can create two slightly asymmetrical semicircles on the Nyquist diagram: one at low frequencies, where the oxygen diffusion dominates the operation of the cell and one at medium frequencies due to the combined effects of the double-layer capacitance and faradaic processes. The second semicircle becomes negligibly small at low values of the cathode width or oxygen concentration. Both semicircles can degenerate into one large semicircle when the double layer capacitance is large enough and masks the effects of the faradaic processes, which happens at large values of the specific area of the cathode and double layer capacitance, or when the oxygen diffusion coefficient in the electrolyte is relatively large. They also degenerate into one semicircle when the porosity is decreased, for instance during the final period of the discharge of Li-air batteries with organic electrolyte, when the cathode is partly clogged with the deposit reaction products. The elements of the small-signal equivalent circuit are expressed in terms of the oxygen diffusion coefficient, oxygen concentration, discharge current, and other material and kinetic parameters, which make our model instrumental for extracting information about the material structure, reaction processes, and diffusion in the cathode. Based on the derived analytical results, we also propose a method to extract the effective value of the oxygen diffusion coefficient and reaction rate constant from the experimental impedance spectra of the cells. A simplified small-signal equivalent circuit model is also presented. This model contains only elementary components such as resistors and capacitors and can be implemented numerically in circuit simulators.
 [DOI: 10.1149/2.046311jes]

Manuscript submitted May 1, 2013; revised manuscript received September 12, 2013. Published September 27, 2013.

Li-air batteries have attracted much attention in the last years particularly because of their high energy densities and specific capacities.[1–3] Depending on the type of the battery, the specific capacity is estimated to vary between 1,000-3,840 mAh/g,[4–6] which is a few times to more than one order of magnitude larger than the energy density of Li-ion batteries. This high specific capacity is mostly due to the fact that Li-air batteries use oxygen from the air instead of storing it internally and lithium metal at the anode instead of a composite material. Additionally, Li-air batteries are environmental safe and provide an oil-independent source of energy, which make them attractive in a broad area of applications including transportation, portable electronic devices, and green energy storage.

Impedance analysis methods are often employed as convenient, nondestructive ways to analyze and predict the performance of batteries and other energy storage devices.[7] These methods can be used to extract information about the reaction and diffusion processes inside electrochemical devices, as well as about the state-of-charge, state-of-health, ohmic losses, and reliability of these devices. For instance, in the case of Li-ion batteries, one can predict the voltage and monitor the state-of-charge of the cells,[8,9] diagnose and investigate the electrochemical properties and determine the values of the Li diffusion coefficient, reaction rate, and other parameters using impedance spectroscopy.[10,11] In the case of proton exchange membrane fuel cells one can use impedance spectroscopy measurements to study the degradation and stability of these cells,[12] and determine the values of the catalyst layer resistance,[13] reaction rates, and proton and oxygen diffusivities.[14,15] In general, to extract these information we need to develop a physics-based model for the total impedance spectra in terms of the material and electrochemical properties of the system, such as the structure, geometry, kinetic, and diffusion parameters, and then fit this model to the experimental data. It is often preferable that the model be given in terms of relatively simple a.c. circuits involving resistors, capacitors, and inductors, whose values are related to the physical properties of the system.[16]

In this article we develop an electrochemical impedance spectra model for Li-air batteries and relate the characteristics of the spectra of these batteries to their geometrical dimensions, kinetic parameters, diffusion coefficient, porosity, and pore structure. We also propose a method to extract the effective value of the oxygen diffusion coefficient and reaction rate constant from the experimental impedance spectra of the cells. The results for the impedance spectra are derived under relatively general assumptions of the structure and type of the battery, by looking at the oxygen diffusion and faradaic processes in the porous cathode. Since the operation of Li-air batteries is dominated by these processes the effects of other phenomena such as the anode reaction rate or ion transport though the electrolyte can be neglected. We expect this model to be valid for a large number of Li-air or Li-oxygen systems, in which the oxygen diffusion-reaction plays a limiting factor. In particular, the model can be applied to primary and secondary Li-air batteries with organic and aqueous electrolytes as we will also discuss in the next section.

Most of the existing work on the theoretical modeling of impedance spectra of electrochemical system is related to the study of Li-ion, other metal-ion or metal batteries, and electrocapacitors, which are dominated by Warburg diffusion or various versions and improvements the Warburg diffusion model (e.g. bounded Warburg models). These models are usually represented in the form of small-signal transmission line circuit models. They are relatively accurate for systems that can be modeled with a semi-infinite or bounded diffusion region and where the reaction takes place on the boundary of this region.[16] However, Warburg diffusion models cannot be applied to Li-air systems with porous cathodes, in which the local concentration of one of the reactants (i.e. oxygen) varies significantly from point to point leading to a large spatial distribution of reaction rates. Such systems contain a diffusion-reaction region that can often be described by Gerischer or modified versions of the Gerischer impedance.[17,18] The Gerischer impedance has been applied to a number of electrochemical systems including batteries and fuel cells[12,19] and has been developed under the assumption of zero d.c. discharge during the small-signal measurement.[20] In this article we develop a reaction-diffusion model for Li-air batteries, in which the impedance spectra are measured under non-zero d.c. discharge. We show that the value of the d.c. discharge current can be used as an additional controlling variable, under which the spectra are measured and, thus, provides additional

*Electrochemical Society Active Member.
zE-mail: pandrei@eng.fsu.edu

information about the physical processes and material properties of the cell.

The article is structured as follows. The first section summarizes the model equations and the approximations that we use to derive the impedance spectra of Li-air batteries. The next section summarizes the closed-form formulas for the electrochemical impedance spectra and presents a general small-signal circuit model for these batteries. The detailed derivation of the impedance spectra is shown in the Appendix. The next section presents approximations for the impedance spectra in the cases of large and small cathode widths and discharge currents and presents a simplified small-signal (a.c.) circuit model for the battery. In addition, it discusses how the values of the circuit elements depend on the physical and electrochemical properties of the system. Concluding remarks are presented in the last section.

Model Equations and Steady-State Analysis

In this section we present the mathematical model and the main approximations that were used to derive the analytical expression for the impedance of lithium-air batteries. The model presented below can be applied to both Li-air batteries with organic and aqueous electrolytes. These batteries are usually composed of a Li metallic anode, a solid separator, and a porous carbon cathode filled with organic or aqueous electrolyte. The space between the anode and the separator is usually filled with a thin organic electrolyte layer. External air penetrates the pores of the cathode from the right, diffuses through the electrolyte, and reacts with the Li ions according to the following reactions (see Fig. 1):[3,4]

Li-air with organic electrolyte:

$$2Li^+ + O_2 + 2e^- \rightarrow Li_2O_{2(\text{deposit})} \quad [1]$$

$$Li^+ + O_2 + e^- \rightarrow LiO_{2(\text{deposit})} \quad [2]$$

Li-air with aqueous electrolyte (before saturation):

$$4Li^+ + O_2 + 2H_2O + 4e^- \rightarrow 4Li^+ + 4OH^- \quad [3]$$

Li-air with aqueous electrolyte (after saturation):

$$4Li^+ + O_2 + 6H_2O + 4e^- \rightarrow 4LiOH \cdot H_2O_{(\text{deposit})} \quad [4]$$

In the case of Li-air batteries with organic electrolyte the reaction product is insoluble in the electrolyte and deposits in the cathode. In the case of Li-air batteries with aqueous electrolyte we distinguish two regimes of operation depending on the concentration of the aqueous electrolyte in the cathode: (a) before saturation when the concentration of Li^+ and OH^- ions is smaller than the concentration of saturation of Li^+OH^- in water, and (b) after saturation when the concentration of Li^+ and OH^- ions is equal to the concentration of saturation of Li^+OH^- in water. When the concentration of Li^+ and OH^- ions reaches saturation, the reaction product $LiOH \cdot H_2O$ deposits on the surface of the carbon, thus filling in the pores of the cathode and eventually interrupting the flow of the O_2 in the cathode. In both types of batteries, when all the pores from the air side of the cathode are clogged or when the resistance of the deposit product at the cathode is too large, reactions 1-4 cannot take place anymore and the battery cannot be further discharged. These are the main reasons for the relatively short life of Li-air batteries.

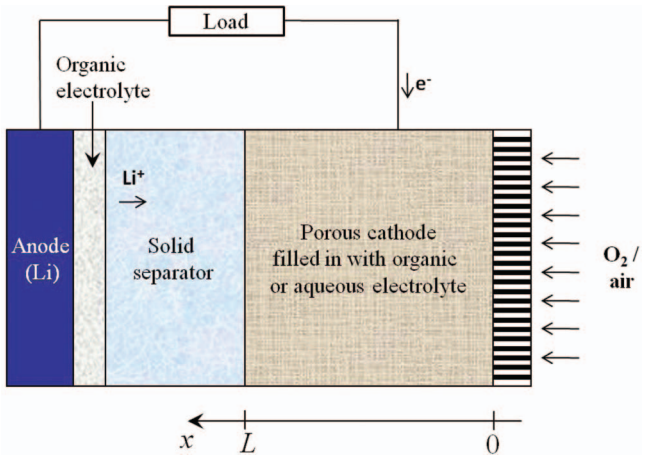

Figure 1. Structure of a Li-air battery system with (a) organic and (b) aqueous electrolyte.

More accurate and complex models for the simulation of Li-air batteries with organic electrolyte been developed by Andrei et al.[21] and Albertus et al.[22] Models for the simulation of Li-air batteries with aqueous electrolyte before and after saturation are presented in Ref. 23. However, due to the increased complexity of these models it is practically impossible to derive any closed-form solutions for the impedance spectra analytically, and one should employ numerical simulations to compute the impedance diagrams.

Basic equations and assumptions.— In order to derive an analytical model for the impendence spectra in Li-air batteries we assume that the discharge of these batteries is limited by the oxygen diffusion in the cathode. This fact has been observed and discussed by a number of authors in the last years and it is commonly accepted that the reduced power density of Li-air batteries is due to the slow oxygen diffusion in the porous cathode material. Considering one-dimensional mass transfer, the oxygen concentration satisfies the following diffusion equation

$$\frac{\partial\left(\varepsilon c_{O_2}\right)}{\partial t} = \frac{\partial}{\partial x}\left(D_{O_2,eff}\frac{\partial c_{O_2}}{\partial x}\right) - \frac{r_C}{2F} \quad [5]$$

where r_C is the specific reaction rate at the cathode, which can be approximated by the following simplified Butler-Volmer (Tafel) equation[24,25]

$$r_C = 2Fkc_{O_2}a\left(\varepsilon\right)e^{-\frac{n\beta}{V_T}\eta},\ \eta < 0\,(\text{discharge}) \quad [6]$$

Note that we have included only the forward reaction current and have neglected the reverse current in the Butler-Volmer equation. This approximation is good when the battery is operated under relatively large discharge currents, but it fails when the battery is either being charged or operated at very low discharge rates such that the forward and reverse currents are comparable to each other. Hence, in the analysis that follows we discuss only about the case when the battery is operated under discharge and eq. 6 holds. The charge transfer coefficient n in eq. 6 is equal to two if the rate-determining step in eqs. 1-4 is a two-electron transfer and is equal to 1 if it is a one-electron transfer. It is important to stress that eq. 6 captures the dependence of the current density on the oxygen concentration only qualitatively and more research is needed to establish the nature of the equilibrium reactions at the cathode exactly. We also prefer to write the reaction rate in form 6 because it can be applied to both Li-air batteries with organic and aqueous electrolytes and, as we will show next, leads to closed-form solutions for the discharge current and impedance spectra. Notice that other similar functional forms for the reaction current also exist in the literature.[22]

An important approximation made in 5 and 6 is that we assume the oxygen concentration at the surface is equal to the oxygen concentration in the middle of the pores, i.e. $\partial c_{O_2}/\partial r \simeq 0$ as also discussed by Sandhu et al.[25] This approximation simplifies the analysis by leading to one-dimensional diffusion equations but can result in some transport phenomena at the solid-electrolyte interface that are being ignored, and which could in principle result in additional features on the impedance spectra diagrams. Such phenomena might include traditional Warburg impedance effects.

It is also worthwhile noting that by using eq. 5 we exclude flow batteries or other Li-air batteries in which the electrolyte in the cathode region is oxygenated by stirring processes. In these types of batteries

convection plays an important role in the oxygen transport and eq. 5 needs to be modified accordingly.

The specific surface area of the cathode depends on the local porosity according to a function, $a(\varepsilon)$. The functional form of this dependence is given by the exact microstructure of the cathode. A few idealized cases are discussed in Appendix A. Factor 2 in eqs. 5 and 6 appears because each molecule of oxygen participating in the cathode reaction produces two electrons.

For the sake of simplicity, the cell voltage v is related to the overvoltage η by

$$v = V_0 + \eta - V_\Omega \quad [7]$$

where V_0 is the open cell voltage and V_Ω denotes the combined voltage drops across the separator, anode and deposit layers, interfaces, and electrolyte; in addition, V_Ω includes any other ohmic losses such as losses at the contacts of losses due to the electron transport in the cathode. In general, we expect for V_Ω to depend on the value of the discharge current. For instance, if the deposit layer at the cathode is insulator, the electrons have to tunnel through this deposit layer and the total current depends nonlinearly on the overvoltage as suggested by a number of recent publications.[3,26,27] Quantum tunneling results in a strongly nonlinear dependence of V_Ω as a function of the discharge current.

Eq. 5 is subject to the following boundary conditions

$$\left.\frac{dc_{O_2}(x,t)}{dx}\right|_{x=L} = 0 \quad [8]$$

$$c_{O_2}(0,t) = C_O^* \quad [9]$$

and initial condition

$$c_{O_2}(x,0) = C_O^* \quad [10]$$

where we have assumed that the oxygen enters at $x = 0$ and diffuses toward the separator, which is located at $x = L$. As it usually done in the literature,[28,29] we assume that the discharge current can be split into a faradaic component, i_F, and a component due to the discharge of the double layer, i_d, and can be computed as

$$i = i_F + i_d = A\int_0^L r_C dx + A\int_0^L aC_d\frac{d\eta}{dt}dx \quad [11]$$

where C_d is the capacitance of the depletion layer per unit area and i_F and i_d refer to the two integrals in eq. 11, respectively.

To derive closed-form equations for the impedance spectra we assume that the porosity of the battery varies slowly in time during discharge and this variation can be neglected during the time the a.c. impedance measurement is performed. Indeed, in Li-air batteries with organic electrolyte the porosity decreases slowly in time when the reaction product deposits on the surface of the carbon. In Li-air batteries with aqueous electrolyte the porosity might change or not in time depending on whether the electrolyte in the cathode is saturated or not. In both cases, the impedance spectra measurements are performed within few seconds or minutes, which is much faster than the lifetime of the battery. In addition, it is convenient to assume that the porosity of the battery is uniformly constant throughout the cathode, which is usually the case when the battery is completely charged or if it was partially discharged at a very low discharge rate. With these assumptions, eq. 5 becomes

$$\varepsilon\frac{\partial c_{O_2}}{\partial t} = D_{O_2,eff}\frac{\partial^2 c_{O_2}}{\partial x^2} - \frac{r_C}{2F} \quad [12]$$

and the cell discharge current

$$i = i_F + i_d = 2AFkae^{-\frac{n\beta}{V_T}\eta}\int_0^L c_{O_2}(x,t)\,dx + AaC_d\int_0^L\frac{d\eta}{dt}dx \quad [13]$$

Steady state (d.c.) analysis.— Let us consider the case of steady-state, i.e. when the time derivatives in eqs. 12 and 13 can be neglected. As mentioned before, during discharge, Li-air batteries are never in a perfect steady-state because the reaction products deposit slowly but continuously in time. However, since the change in porosity is very slow in time we can approximate that the battery is at steady-state during the time the impedance spectra are measured. Next, we denote the steady-state value of the overvoltage by η_0 and the steady-state values of all other quantities using capital letters; for instance $C_{O_2}(x)$ is the d.c. oxygen concentration, I is the d.c. value of current i, etc. The oxygen diffusion equation at steady-state is

$$\frac{\partial^2 C_{O_2}}{\partial x^2} - \frac{ka}{D_{O_2,eff}}C_{O_2}e^{-\frac{n\beta}{V_T}\eta_0} = 0 \quad [14]$$

with the following solution

$$C_{O_2}(x) = C_{O_2}^*\left[\cosh\left(\frac{x}{\lambda}\right) - \tanh\left(\frac{L}{\lambda}\right)\sinh\left(\frac{x}{\lambda}\right)\right] \quad [15]$$

where we have used boundary conditions 8 and 9 and introduced notation

$$\lambda = \sqrt{\frac{D_{O_2,eff}}{ka(\varepsilon)}e^{\frac{n\beta}{V_T}\eta_0}} \quad [16]$$

Function $C_{O_2}(x)/C_{O_2}^*$ is represented in Fig. 2 for different values of the λ parameter. Parameter λ characterizes the diffusion length of oxygen in the cathode (for instance, if $L \gg \lambda$, λ represents the distance after which the oxygen concentration is decreased by 31%).

The discharge current at steady-state is equal to the faradaic current and can be evaluated from eq. 13

$$I = 2AFka(\varepsilon)C_O^*e^{-\frac{n\beta}{V_T}\eta_0}\int_0^L\left[\cosh\left(\frac{x}{\lambda}\right) - \tanh\left(\frac{L}{\lambda}\right)\sinh\left(\frac{x}{\lambda}\right)\right]dx \quad [17]$$

which leads to the following condition between the d.c. discharge current and λ

$$\frac{I\lambda}{2AFD_{O_2,eff}C_O^*} = \tanh\left(\frac{L}{\lambda}\right) \quad [18]$$

Equations 16 and 18 are important because they allow us to compute the steady-state (d.c.) current when the overvoltage is given. Indeed, if η_0 is given we can compute λ from 16, and the steady-state current I from 18. Alternatively, if the discharge current I is given, we can compute λ by solving nonlinear equation 18 and η_0 from 16. Hence, η_0 can always be expressed as a function of I, i.e. $\eta_0(I)$. Eq. 18 can also be regarded as an expression for the oxygen diffusion length parameter λ as a function of the discharge current I. For large cathode

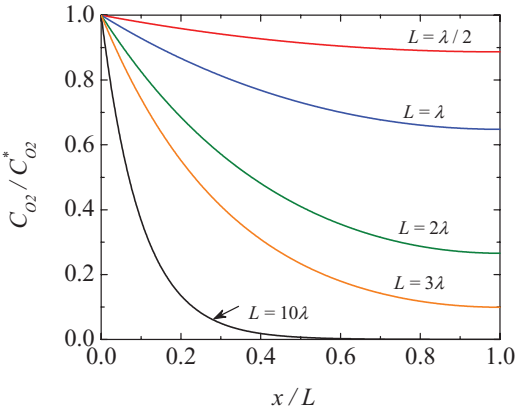

Figure 2. Oxygen concentration as a function of the distance from the oxygen boundary.

widths, we obtain

$$\lambda = \frac{2AFD_{O_2,eff}C_O^*}{I}, \text{ when } L/\lambda \to \infty \quad [19]$$

which shows that to increase the diffusion length of the oxygen in the cathode we need to either increase the effective diffusion coefficient of the oxygen or the oxygen concentration at $x = 0$.

General Expression for Impedance Spectra

The impedance spectra can be computed by superposing a small a.c. signal perturbation $\tilde{v}e^{j\omega t}$ to the d.c. value of the applied voltage and computing the variation of the cell current $\tilde{i}e^{j\omega t}$. Indeed, any small variation in the cell voltage $\tilde{v}e^{j\omega t}$ translates into small variations of the overvoltage $\tilde{\eta}e^{j\omega t}$, faradaic and double-layer currents, and a variation $\tilde{c}_{O_2}(x)\,e^{j\omega t}$ of the oxygen concentration, where $\tilde{\eta}$, $\tilde{v}$, and $\tilde{i}$ are complex numbers, while $\tilde{c}_{O_2}$ is a complex function that needs to be determined. If we explicitly separate the d.c. from the a.c. parts of the signals we can write

$$v = V + \tilde{v}e^{j\omega t} \quad [20]$$

$$i = I + \tilde{i}e^{j\omega t} \quad [21]$$

$$i_F = I_F + \tilde{i}_F e^{j\omega t} \quad [22]$$

$$i_d = I_d + \tilde{i}_d e^{j\omega t} \quad [23]$$

$$\eta = \eta_0 + \tilde{\eta}e^{j\omega t} \quad [24]$$

By superimposing an a.c. signal over different d.c. discharge currents we are actually considering the case a.c. voltammetry. The total impedance can be computed using eq. 7; we obtain:

$$Z = -\frac{\tilde{v}}{\tilde{i}} = \frac{R_\Omega\tilde{i} - \tilde{\eta}}{\tilde{i}} = R_\Omega - \frac{\tilde{\eta}}{\tilde{i}_F + \tilde{i}_d} = R_\Omega - \frac{\tilde{\eta}}{\tilde{i}_F + j\omega aLAC_d\tilde{\eta}}$$

$$= R_\Omega + \frac{Z_F}{1 + j\omega C_D Z_F} \quad [25]$$

where

$$R_\Omega = -\frac{\partial V_\Omega}{\partial I} \quad [26]$$

$$C_D = aLAC_d \quad [27]$$

are the small-signal ohmic resistance and double layer capacitance, and $Z_F = -\frac{\tilde{\eta}}{\tilde{i}_F}$ is the faradaic component of the impedance. The negative sign in the first equation in 25 and in eq. 26 appears because any increase in the cell voltage results in a decrease of the cell current during the discharge of the cell. In writing 25 we have assumed that the capacitance of the double layer does not depend significantly on the discharge current, and the derivative $\frac{\partial C_d}{\partial I}$ can be neglected with respect to the other terms. This fact as a good approximation as indicated by previous experimental results by Baert et al.[30]

It is shown in Appendix B that the faradaic impedance depends on the discharge current I and frequency as

$$Z_F(I,\omega) = \frac{V_T}{n\beta I} \times F\left[\frac{\omega\varepsilon\lambda(I)^2}{D_{O_2,eff}}, \frac{L}{\lambda(I)}\right] \quad [28]$$

where we have introduced function

$$F(\Omega, l) = \frac{j\Omega}{\frac{\tanh\sqrt{1+j\Omega}l}{\sqrt{1+j\Omega}\tanh l} + j\Omega - 1} \quad [29]$$

and have indicated explicitly that λ is a function of the discharge current I (see eq. 18). Function F is complex and depends on the discharge current and cathode length. Nyquist plots and approximate expressions for this function at large and low discharge currents, frequencies, and cathode lengths are given in Appendix C.

Equations 25-29 represent the general form of the impedance of Li-air batteries as a function of the discharge current, reaction rate parameter, oxygen diffusion coefficient, capacitance of the double layer, porosity, and geometrical dimensions. If the discharge current is known we can compute λ from eq. 18, Z_F from 28 and 29, and the total impedance Z from 25. It is worthwhile comparing result 29 to the Gerischer impedance $Z_G(\Omega) = \frac{1}{\sqrt{1+j\Omega}}$ or the finite length Gerischer impedance[20] $Z_G(\Omega) = \frac{\tanh\sqrt{1+j\Omega l}}{\sqrt{1+j\Omega}}$, which were obtained under the assumption that the d.c. value of the discharge current is zero.[20] All these expressions contain the same functional term $\sqrt{1+j\Omega}$, which seems to be characteristic to diffusion-reaction processes in general, and result in relatively similar spectra. However, the expression of the normalized frequency Ω is different in eq. 29 from the expression that appears in the Gerischer impedance. In addition, the Nyquist plot of the Gerischer spectra starts at an angle of approximately 45 degrees at high frequencies, while expression 29 leads to a much more abrupt slope, close to 90 degrees. The relatively high initial slope is also evidenced by recent experimental results on Li-air systems.[31] The equation for the Gerischer impedance cannot be derived as a limiting case of eq. 29 at low currents, because the assumptions that were made in deriving 29 do not hold at low discharge currents; in particular, the reaction rate in expression 6 is valid only when the overvoltage is much higher than the thermal voltage.

The validity of our results 25-29 is expected to depend on how accurately the system can be described by eqs. 5 and 6. Hence, the model will not be appropriate when the spectra are measured under zero or low d.c. discharge current or when the electrolyte is stirred. We also expect the model to fail when the cathode porosity is not uniform, for instance when the discharge product is deposited nonuniformly throughout the cathode.

For the remaining of this section we present numerical results for a standard Li-air battery with the parameters specified in Table I and discuss the conditions under which the faradaic impedance Z_F is hidden by other effects induced by the double layer capacitance. These parameters were either computed or taken from the literature. The reaction constant was estimated such that the specific reaction rate constant, $a(\varepsilon)k$ is in agreement with previous simulations.[21] The capacitance of the double layer depends on the type of the electrolyte

Table I. Values for the parameters Li-air batteries with organic and aqueous electrolyte.

Parameter	Value	Units	Reference
D_{O_2} (organic electrolyte)	7×10^{-6}	cm^2/s	2
D_{O_2} (aqueous electrolyte)	1.3×10^{-5}–5.5×10^{-5}	cm^2/s	35
brugg	1.5	cm^2/s	21
L	0.01	cm	31
A	1	cm^2	Assumed
C_O^*	3.26×10^{-6}	mol/cm^3	Calculated*
a	10^4	cm^2/cm^3	21
n	2		31
β	0.5		Assumed
ε	0.75		Assumed
C_d	10	$\mu F/cm^2$	Assumed
I	1	mA/cm2	
k	1.3×10^{-8}	cm/s	21

*Calculated assuming the external oxygen concentration in air is $9.46\ 10^{-6}$ mol/cm^3 air and the solubility factor is 0.345

and usually ranges between 10 μF/cm^2 and 30 μF/cm^2. In the computations presented in this section we used $C_d = 10$ μF/cm^2, in order to emphasize the effects of the faradaic component of the impedance and also be able to compare with recent results by Adam et al.,[31] who found that the capacitance of the double layer in Li-air batteries can be as low as 7 μF/cm^2. However, computations for larger capacitances are also presented. The oxygen diffusion coefficient was considered equal to the value in organic electrolyte. To investigate the effect of various parameters on the impedance spectra we plot the Nyquist diagrams by varying one or more of these parameters while keeping the remaining parameters fixed. The angular frequency is always varied from 1 mHz to 1 MHz. To simplify the analysis we assume $R_\Omega = 0$ in eq. 25, but one can easily introduce the effect of R_Ω by properly shifting the Nyquist diagram along the horizontal axis. Resistance R_Ω can depend significantly on the type of the battery and includes the resistance of the electrolyte, contacts, deposit layer in the cathode, and also the effects of the anode or anode-separator interface. These additional effects are neglected in this section but we will re-consider them in the next section when we discuss a small-signal equivalent circuit.

A parameter that modifies the shape of the impedance spectra significantly is the specific area of the cathode that, depending on the material and fabrication process of the cathode, can change over a few orders of magnitude from $a = 10^3$ cm^2/cm^3 to 10^5 cm^2/cm^3 or even more. As it will be shown in this article, the specific area directly affects the total capacitance of the double layer, C_D, and can hide the effects of the faradaic impedance. Hence, we will present and discuss the results for the cases when $a = 10^4$ cm^2/cm^3 and $a = 10^5$ cm^2/cm^3 separately.

Fig. 3 presents the Nyquist diagram of the impedance for different values of the discharge current ranging from 0.2 mA/cm^2 to 5 mA/cm^2 and for two specific areas of the cathode, $a = 10^4$ cm^2/cm^3 and $a = 10^5$ cm^2/cm^3. As shown in these figures and also suggested by eq. 28 the magnitude of the impedance spectra decreases proportionally with the value of the discharge current. For currents smaller than 0.1 mA/cm^2, the approximation of using the Tafel equation instead of the complete Butler-Volmer equation does not hold and we expect the magnitude of the impedance spectra to saturate at some point if the current is decreased even more. All the impedance spectra have a capacitive behavior (i.e. Im $(Z_F) < 0$) and become purely resistive when $\omega \to 0$ or $\omega \to \infty$. The Nyquist diagram shows two semicircles, one at medium frequencies due to the existence of the double layer and one at low frequencies due to the mass transport of the oxygen. At large discharge currents, the two semicircles merge with each other because the faradaic impedance Z_F become negligible and the total impedance is dominated by the capacitance of the double layer. It is important to note that by increasing the specific area of the cathode the faradaic effects are hidden by the capacitance of the double layer and the two semicircles will merge into one bigger semicircle on the Nyquist plot. This shows that in order to be able to observe the effects of the faradaic impedance derived in eq. 28 we need to use cathodes with relatively low specific area of the cathode and high reaction rate constants; otherwise the faradaic effects are masked by the charge transfer and double layer capacitance.

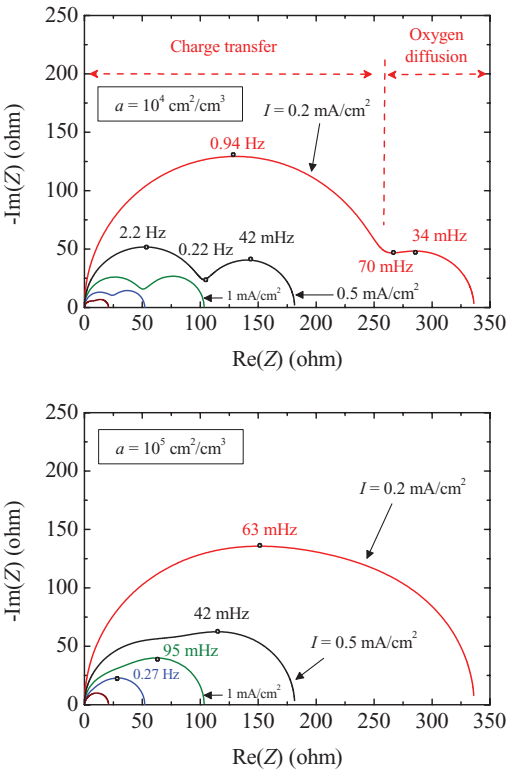

Figure 3. Nyquist plot of the cathode impedance at different values of the discharge current I (from bottom to top $I = 5$ mA, 2 mA, 1 mA, 0.5 mA, and 0.2 mA) for two separate specific areas of the cathode.

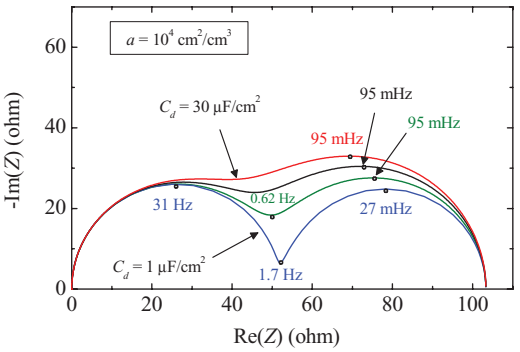

Figure 4. Nyquist plot of the cathode impedance for different values of the double layer capacitance C_d (from bottom to top $C_d = 1$ μm/cm^2, 10 μm/cm^2, 20 μm/cm^2, and 30 μm/cm^2).

Next, we investigate the effects of the capacitance of the double layer on the total impedance of the battery. Fig. 4 shows the Nyquist diagram for four values of C_d, ranging from 1 μF/cm^2 (which can be considered a negligible capacitance) to 30 μF/cm^2. The effect of the capacitance of the double layer is to hide the effects of the faradaic impedance Z_F. For values of C_d larger than 20 μF/cm^2, Z_F becomes negligible even for relatively low values of the specific area.

It is known that the performance of the Li-air batteries is limited by the relatively low diffusion coefficient of the oxygen in the cathode electrolyte and, in order to improve the power density of these batteries, it is imperative to increase this diffusion coefficient. Hence, Fig. 5 shows the Nyquist diagram for various values of the oxygen diffusion coefficient, starting from 10^{-7} cm^2/s to 2.4×10^{-5} cm^2/s. It is worthwhile noting that the low frequency semicircle vanishes for large values of the diffusion coefficient and is masked by the double layer capacitance for small values. For this reason, it is easier to observe the above features of faradaic impedance in organic Li-air batteries, which have a slightly lower diffusion coefficient than the aqueous batteries. Fig. 6 shows the Nyquist diagram for three values of the oxygen concentration ranging from $C_O^* = 7.1 \times 10^{-7}$ mol/cm^3 to 1.4×10^{-5} mol/cm^3; the lowest value corresponds to a 5% oxygen concentration while the highest value to 100% oxygen at 1 atm and room temperature. Large values of the oxygen concentration can improve the power density of Li-air batteries and can be obtained particularly in flow batteries.[32] It is apparent from Fig. 6 that the impedance spectra can change significantly as a function of the oxygen concentration, particularly for low specific areas. The effect of the oxygen concentration is somewhat similar to the effect of the oxygen diffusion coefficient, in the sense that the faradaic impedance becomes noticeable for a limited range of value of the oxygen concentration.

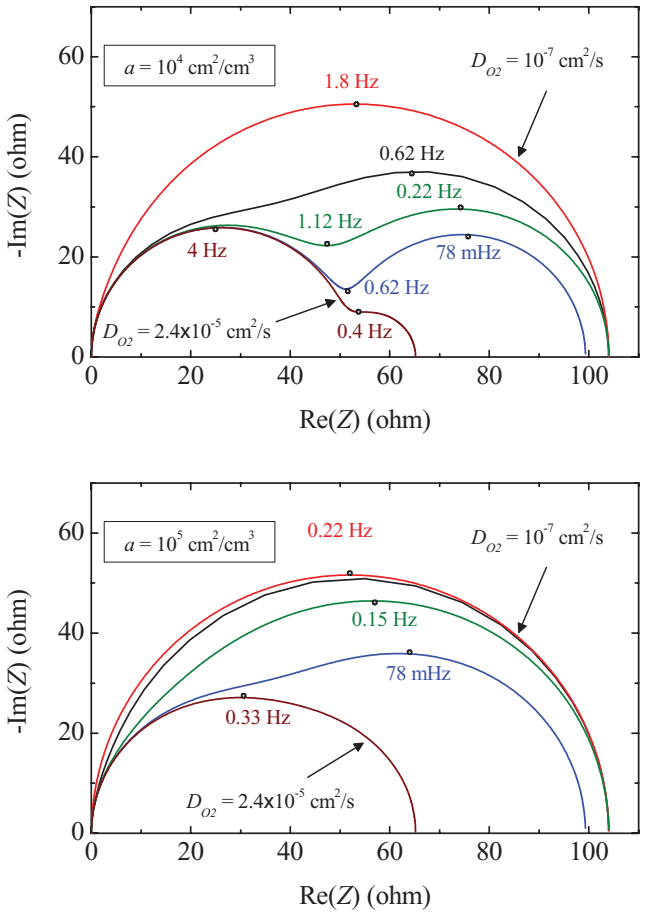

Figure 5. Nyquist plot of the cathode impedance for different values of the oxygen diffusion coefficient D_{O_2} (from bottom to top $D_{O_2} = 2.4 \times 10^{-4}$ cm^2/s, 10^{-5} cm^2/s, 3×10^{-6} cm^2/s, 10^{-6} cm^2/s, and 10^{-7} cm^2/s) for two separate specific areas of the cathode.

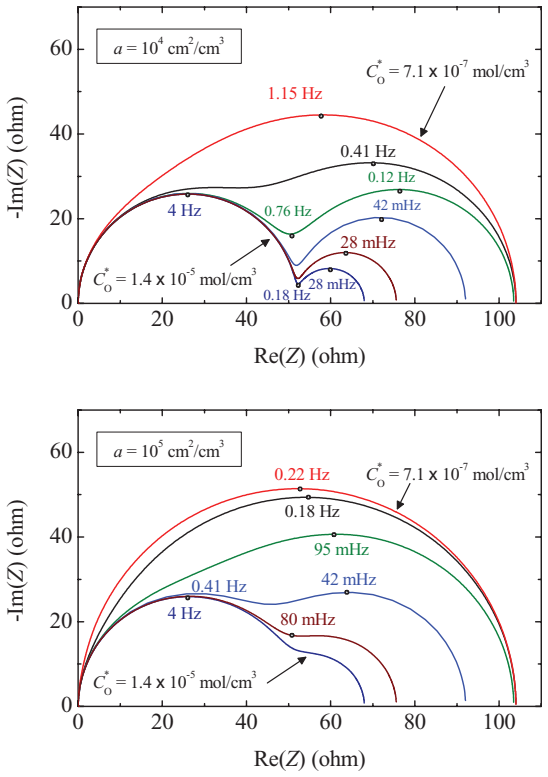

Figure 6. Nyquist plot of the cathode impedance for different values of the oxygen concentration C_O^* (from bottom to top $C_O^* = 1.4 \times 10^{-5}$ mol/cm^3, 9.9×10^{-6} mol/cm^3, 5.6×10^{-6} mol/cm^3, 2.8×10^{-6} mol/cm^3, 1.4×10^{-6} mol/cm^3, and 7.1×10^{-7} mol/cm^3) for two separate specific areas of the cathode.

Fig. 7 shows the Nyquist diagram for different values of the porosity equal to $\varepsilon = 0.4$. 0.5, 0.6, 0.7, 0.8, and 0.9. The specific area of the cathode is kept constant and equal to $a = 10^4$ cm^2/cm^3 and $a = 10^5$ cm^2/cm^3 for the simulations shown in Fig. 7a and Fig. 7b respectively. These computations correspond to the case of Li-air batteries with organic electrolyte when the deposit layer is decreasing the porosity. Notice that the effects of the faradaic impedance Z_F are suppressed during the deposition of the cathode material, which suggests that the faradaic impedance can be used as a way to determine the state-of-charge of the battery. These results predict that the diameter of the semicircles created by the cathode on the Nyquist plot should slightly increase while the battery is being discharged.

Fig. 8 shows the Nyquist diagram for various values of the cathode length varying from $L = 50$ μm to 0.12 mm and for the same two values of the specific area. The effect of increasing the cathode length is somewhat equivalent to decreasing the diffusion coefficient or the oxygen concentration in the cathode, however, the corresponding frequencies on the Nyquist diagram are different (compare Fig. 5 with Fig. 8). For cathode lengths larger than 2 mm (not shown in the figure) the cathode length does not influence the shape of the impedance diagram and the Nyquist plot displays one semicircle due to the double layer.

Depending on the exact reaction steps and on the final reaction products (e.g. LiO_2, Li_2O_2, $LiOH \cdot H_2O$, etc.) the number of electrons involved in the chemical reaction can vary. Hence, Fig. 9 shows the Nyquist diagram for five values of the charge transfer coefficient, $n = 1$, 1.5, 2, 3, and 4. The effect of increasing the charge transfer

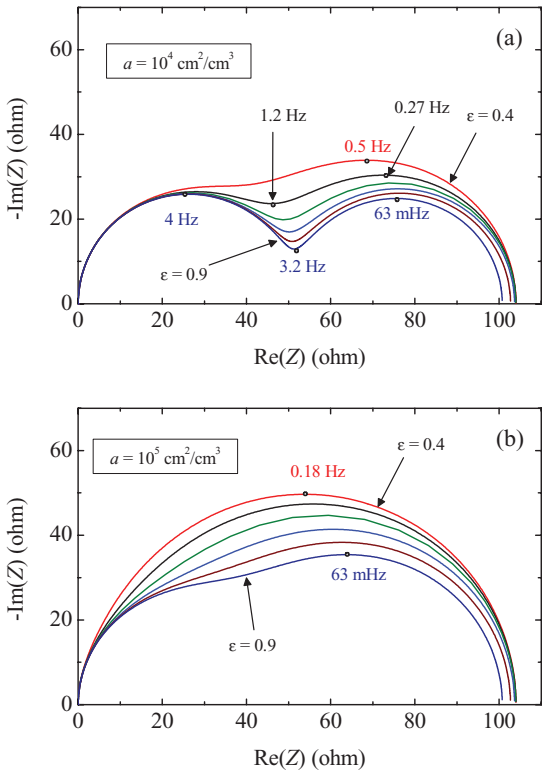

Figure 7. Nyquist plot of the cathode impedance for different values of the porosity ε (from top to bottom ε = 0.4, 0.5, 0.6, 0.7, 0.8, and 0.9) for two separate specific areas of the cathode.

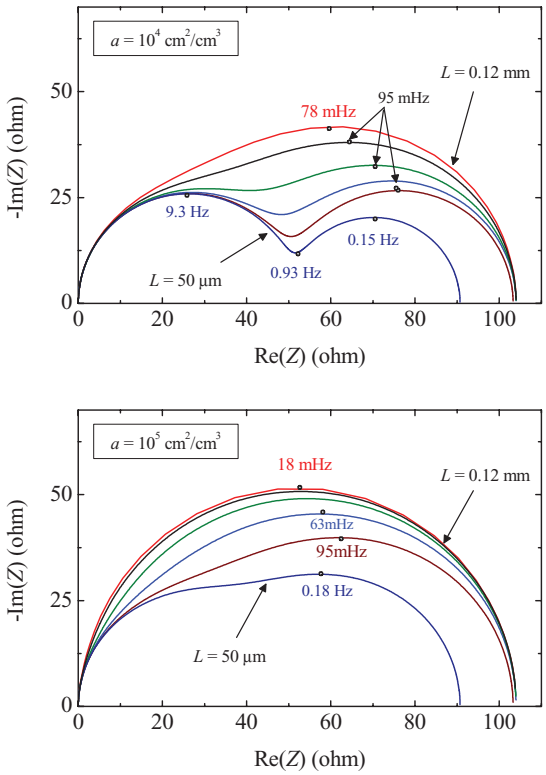

Figure 8. Nyquist plot of the cathode impedance for different cathode thicknesses L (from bottom to top $L = 50$ μm, 100 μm, 200 μm, 400 μm, 800 μm, and 0.12 mm) for two separate specific areas of the cathode.

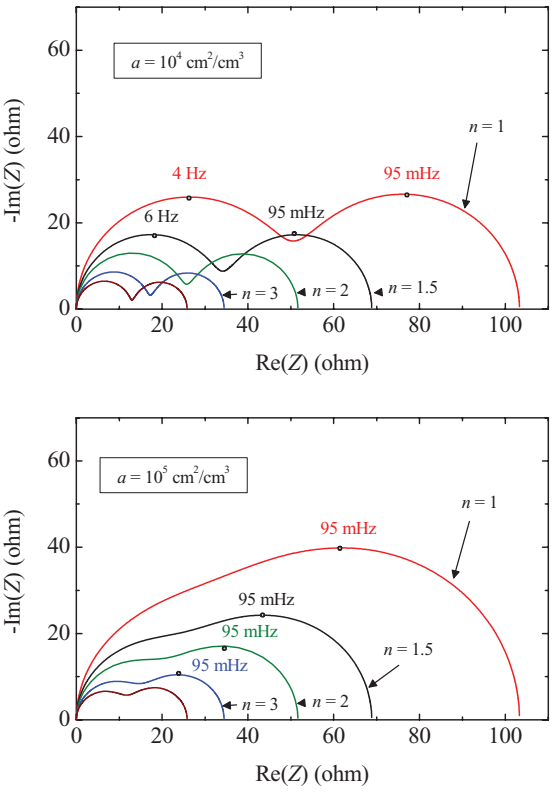

Figure 9. Nyquist plot of the cathode impedance for different values of the charge transfer coefficient n (from bottom to top $n = 4$, 3, 2, 1.5, and 1) and two separate specific areas of the cathode.

coefficient is mostly to decrease the magnitude of the Nyquist plot as shown by these results.

Finally, it is worthwhile summarizing some of the characteristics of the spectra given by eqs. 28 and 29.

1. First, the impedance at low frequencies is resistive and does not have a capacitive behavior like in the case of Warburg impedance. This is a characteristic of the fact that the measurements are performed under d.c. discharge.
2. Second, the slope of the impedance curve on Nyquist plots at high frequencies is close to 90 degrees, and is different from the slope of 45 degrees as predicted by the Gerischer or Warburg impedances, which were obtained under zero d.c. discharge currents.
3. If the specific area of the cathode is small enough so the double layer capacitance is negligible and does not mask the faradaic component of the impedance, the cathode diffusion-reaction layer creates two low frequency semicircles on the Nyquist plot diagram (notice that, the anode and anode-separator interface can create additional semicircles on the diagram). The diameter of the first semicircle is $R = \frac{V_T}{n\beta I}$ and depends on the type of the electrolyte (through the charge transfer coefficient, n); this diameter is inversely proportional to the d.c. discharge current, I, and does not depend on the oxygen concentration. The diameter of the second semicircle varies between 0 and R and depends on the operating conditions and cathode properties.
4. If the specific area of the cathode is large enough the double layer capacitance hides the faradaic effects by creating one large semicircle with the diameter between R and $2R$, depending on the relative oxygen diffusion length in the cathode, l. The diameter of this semicircle is inversely proportional to the d.c. discharge current, is independent on the cathode fabrication technique and might depend slightly on the type of the electrolyte in the cathode, through the charge transfer coefficient, n. At large discharge currents, this diameter becomes equal to $2R$ and does not depend on the value of the oxygen concentration because $l \gg 1$; at low discharge currents the oxygen concentration affects parameter l (see eq. 18) and the diameter of the semicircle can decrease to the lower limit R.

As we will present in the next section, it is remarkable that all of the above characteristics were recently observed experimentally by Adams et al.[31] who measured the impedance spectra of Li-air batteries with organic electrolyte for a variety of oxygen concentrations, separators, and electrolytes.

Small-Signal Equivalent Circuit and Parameter Determination

In this section we focus on establishing the small-signal equivalent circuit for Li-air batteries and developing a parameters determination technique for the model. Eq. 25 shows that the total impedance of the circuit can be represented as a resistor R_Ω in series with a parallel combination of the double-layer capacitance with impedance Z_F

$$Z = R_\Omega + \frac{1}{j\omega C_D} \| Z_F \qquad [30]$$

where R_Ω represents the resistance of the electrolyte and also includes the effects of the anode and anode-separator interface, which might play a significant role in Li-air batteries as suggested by recent experimental results by Adams et al.[31] In such cases R_Ω might be modeled with resistors in series with one or more parallel resistor-capacitor (or constant phase element) pairs connected in series.

The circuit corresponding to model 30 is represented in Fig. 10. In this circuit, the faradaic impedance Z_F is given in terms of the geometric and material properties of the battery by equations 28-29. This circuit can be compared to the standard Randles equivalent circuit.

Next, we present a technique to extract information about the reaction rate, specific surface area, ohmic dissipation, and effective

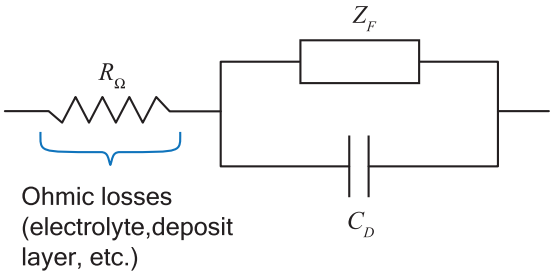

Figure 10. Small-signal equivalent circuit of Li-air batteries. Z_F denotes the faradaic impedance given by eq. 28-29, C_D is the capacitance of the double layer, R_Ω is the combined resistance of the electrolyte, Li-ions, and electrons in the cathode matrix.

diffusion coefficient in the cathode. Depending on whether the faradaic impedance is masked or not by the double layer capacitance we distinguish two cases: (1) the case when the effects of the faradaic impedance are separated from the effects of the double layer capacitance so the Nyquist plot present two different semicircles corresponding to the cathode diffusion-reaction layer, and (2) the case when the effects of the faradaic impedance are hidden by the effects of the double layer capacitance and the Nyquist plot presents only one large semicircle corresponding to the cathode diffusion-reaction region. The first technique is more accurate as it uses more experimental data from the Nyquist plot, however, if the specific area of the cathode is larger than 10^4 cm^2/cm^3 it might be impossible to identify the two semicircles, in which case one needs to use the second technique. In this section we assume that all the other semicircles corresponding to the anode or anode-separator interface have been eliminated from the Nyquist plot.

Parameter determination at low cathode specific areas.— When the specific area of the cathode is relatively low the impedance spectra present two semicircles, one due to oxygen diffusion and the other to charge transfer, as shown in Fig. 11a. To find equations for the effective oxygen diffusion coefficients and reaction rate it is instrumental to replace 28 into 30 and re-write it into normalized form as

$$Z = R_\Omega + \frac{RF\left(\omega/\omega_0, L/\lambda\right)}{1 + j\omega RC_D F\left(\omega/\omega_0, L/\lambda\right)} \qquad [31]$$

where

$$R = \frac{V_T}{n\beta I} \qquad [32]$$

$$\omega_0 = \frac{D_{O_2,eff}}{\varepsilon\lambda^2} \qquad [33]$$

and λ can be computed from the d.c. discharge current using eq. 18. Using the mathematical properties of function F presented in Appendix C, one can show that:

$$\lim_{\Omega\to 0} Z = R_\Omega + R\frac{2\sinh 2l}{\sinh 2l + 2l} \qquad [34]$$

$$\lim_{\Omega\to \infty} Z = R_\Omega \qquad [35]$$

where

$$l = \frac{L}{\lambda} \qquad [36]$$

If we denote the values of the impedance at very low frequencies ($\omega \to 0$) by Z_0 and at very high frequencies ($\omega \to \infty$) by Z_∞, equation 31 becomes

$$Z = Z_\infty + \frac{F\left(\omega/\omega_0, L/\lambda\right)}{\frac{2\sinh 2l}{(Z_0 - Z_\infty)\sinh 2l + 2l} + j\omega C_D F\left(\omega/\omega_0, L/\lambda\right)} \qquad [37]$$

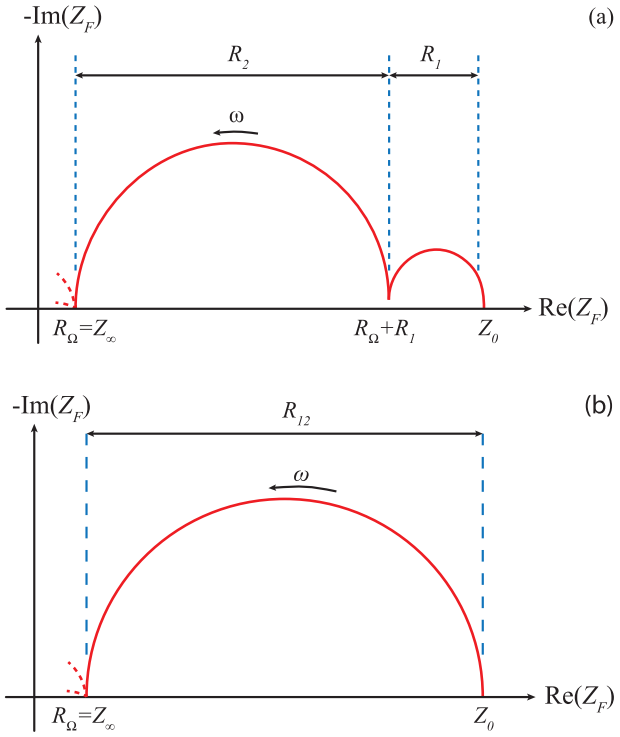

Figure 11. Possible low frequency impedance spectra of Li-air batteries with low specific area of (a) and high specific area of the cathode (b). The dashed lines show that the Nyquist spectra might contain other semicircles at high frequencies, which are usually due to the anode and anode-separator interface.

The last equation needs to be fitted to the experimental impedance spectra to compute Z_0, Z_∞, C_D, ω_0, and λ. Once these parameters are determined one can use the value of λ to extract the effective oxygen diffusion coefficient

$$D_{O_2,eff} = \frac{I\lambda}{2AFC_O^*}\coth\left(\frac{L}{\lambda}\right) \qquad [38]$$

If one can estimate the value of the overvoltage η_0 from d.c. measurements the reaction rate (product ka is expressed in s^{-1}) can be computed using:

$$ka = \frac{D_{O_2,eff}}{\lambda^2} e^{\frac{n\beta}{V_T}\eta_0} \qquad [39]$$

which can be derived from 16. When fitting eq. 37 to experimental data it is important to note that most fitting parameters can be determined with relatively little effort. Indeed, Z_0 and Z_∞ are the low and high frequencies impedances and can be read directly from the data, while parameter λ can be computed using the ratio of the diameter of the low frequency semicircle to the diameter of the high frequency semicircle (see notations in Fig. 11a), i.e.:

$$\frac{R_1}{R_2} = \frac{1}{\frac{1}{2} + \frac{l}{\sinh 2l}} - 1 = \frac{\sinh 2l - 2l}{\sinh 2l + 2l} = \frac{\sinh 2L/\lambda - 2L/\lambda}{\sinh 2L/\lambda + 2L/\lambda} \qquad [40]$$

which can be derived from eq. C4, Appendix C.

To summarize the parameter determination technique, one first computes ratio L/λ by solving nonlinear eq. 40, then the effective oxygen diffusion coefficient from 38 and the reaction rate from 39. The remaining two parameters, C_D and ω_0, can be identified using nonlinear least-square estimations or alternative numerical techniques.

Parameter determination at high cathode specific areas.— When the specific area of the cathode is relatively high the faradaic component of the impedance is masked by the high capacitance of the double layer and the impedance spectrum of the cathode presents only one semicircle as shown in Fig. 11b. In this case, eqs. 37-39 still hold, however, one cannot identify R_1 and R_2 using eq. 40. In this case it

is more convenient to determine resistance R_{12} from the experimental spectra and use the following equation

$$R_{12} = \frac{V_T}{n\beta I}\frac{2\sinh 2l}{\sinh 2l + 2l} = \frac{V_T}{n\beta I}\frac{2\sinh 2L/\lambda}{\sinh 2L/\lambda + 2L/\lambda} \quad [41]$$

In this case, one computes ratio L/λ by solving eq. 41 and, then, the effective oxygen diffusion coefficient from and the reaction rate using 38 and 39, respectively. It should be noted that in order to compute L/λ from eq. 41 one needs to know the value of charge transfer coefficient, n; this coefficient can be computed either using discharge curves or by fitting the experimental and theoretical values of frequency ω_0.

Next, we apply the technique presented above to the modeling of impedance spectra in a Li-air batteries, by comparing our theoretical predictions to experimental data by Adams et al.,[31] who measured the impedance spectra for rechargeable Li-air batteries with cathodes made using different fabrication techniques: separate cast and dual cast cathodes with soaked and embedded electrolytes, room temperature ionic liquid embedded cathodes, and PFTE-calendered cathodes.

The capacitance of the diffusion layer $C_d = 7$ μF/cm^2 and the specific area of the cathode $a = 5 \times 10^4$ cm^2/cm^3 were measured experimentally. The high value of the specific area of the cathode show that the double layer hides the faradaic impedance by creating one semicircle at low frequencies with the diameter equal to R_{12}. Hence, we identified $Z_0 = 19$ Ω and $Z_\infty = 570$ Ω from the experimental data, and solved eq. 41 to compute $l = L/\lambda = 1.96$. For a cathode with $L = 0.01$ mm (such as the one used in Ref. 31), eq. 38 gives an effective value of the diffusion coefficient of $D_{O_2,eff} = 5.6 \times 10^6$ cm^2/s. For a standard cathode with porosity $\varepsilon = 75\%$ and Bruggeman coefficient of 1.5, $D_{O_2} = 8.6 \times 10^6$ cm^2/s, which is in good agreement with predictions by Read et al.[2] who obtained $D_{O_2} = 7 \times 10^6$ cm^2/s. Our theoretical predictions are compared to experimental data in Fig. 12. The frequency was varied between 1 mHz and 1 MHz in agreement with the experimental data. The low frequency points were not used in the parameter determination because, as mentioned by the authors, those points were subject to high experimental errors due to the long measurement time. Notice that the experimental spectra do not start with a slope of 45 degrees at high frequencies like in the case of traditional Gerischer type spectra but at a much higher slope as predicted by our analytical results. The high frequency semicircle of the cell simulated in Fig. 12 is due to the anode-separator interface and we have modeled it with a constant phase element $1/(j\omega)^\alpha Q$, where parameters $\alpha = 0.8$ and $Q = 8.2 \times 10^{-3}$ were measured experimentally.[31]

Our analytical model predicts the experimental values of resistance R_{12} (which is denoted as R_2 in Ref. 31) remarkably well. Indeed, at relatively large discharge currents, eq. 18 predicts large values for l, so $R_{12} = \frac{2V_T}{n\beta I}$. Hence, for a d.c. discharge current of 0.1 mA/cm^2 and $n = 2$, we obtain $R_{12} = 1$ KΩ, which agrees very well with the value of (1 ± 0.02) KΩ presented in Fig. 14 from Ref. 31. At a discharge current of 0.6 mA/cm^2, by keeping the same value of the charge transfer coefficient $n = 2$, we obtain $R_{12} = 166$ Ω, which agrees relatively well with the value of (145 ± 25) Ω data from the same reference. The slight overestimate in the value of R_{12} is due to the fact that in reality n is slightly increasing with the value of the discharge current. In addition, it was shown experimentally that at relatively large discharge currents the values of this resistance do not depend on the cathode fabrication technique and oxygen concentration, in agreement with our theoretical predictions. At low discharge currents, the value of l become sensitive to the oxygen concentration and can vary from $l = \infty$ when the oxygen concentration is large to $l = 0$ when the oxygen concentration is very small. Hence, by decreasing the oxygen concentration one can double the value of R_{12} from R to $2R$ (as implied by 41 and C4). This effect is clearly observed in the experimental data presented Ref. 31, where R_{12} increases from 860 Ω to 1570 Ω when the oxygen concentration is decreased from 100% to 5%.

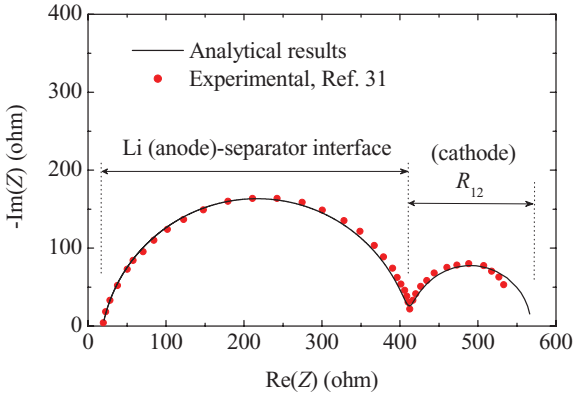

Figure 12. Comparison between the theoretical and experimental impedance spectra. R_1 and R_2 are the diameters of the two semicircles along the real axis and can be used to determine the effective value of the oxygen diffusion coefficient and the reaction rate in the cathode using equations 38-40.

Approximations for the Impedance Spectra and Small-Signal Equivalent Circuit

Depending on the value of $\frac{L}{\lambda}$ it is worthwhile investigating two special cases: one for large currents and cathode widths ($L \gg \lambda$) and the other one for small currents and cathode widths ($L \ll \lambda$). The condition $L \gg \lambda$ implies that

$$\frac{IL}{A} \gg 2FD_{O_2,eff}C_O^* \quad [42]$$

which can be obtained directly from 18. For instance, in the case of Li-air batteries with organic electrolyte if we use Bruggeman condition $D_{O_2,eff} = \varepsilon^{brugg} D_{O_2}$ this condition implies (see values given in Table I)

$$\frac{IL}{A} \gg 4.4 \times 10^{-6} \left[\frac{\text{A}}{\text{cm}}\right] \quad [43]$$

This condition is often satisfied during the normal operation of Li-air batteries particularly when the discharge current and cathode widths are large enough. Therefore, we consider this case in detail in the next section.

Cells with large cathode widths and operating at large discharge/charge currents.— If both the cathode width and discharge current are large enough so that condition 42 is satisfied, $l \gg 1$ and the total faradaic impedance can be approximated to

$$Z_F \simeq \frac{V_T}{n\beta I}\frac{j\Omega}{j\Omega - 1 + \frac{1}{\sqrt{1+j\Omega}}} \quad [44]$$

The last equation was derived using the approximations presented in Appendix C. The Nyquist diagram of the faradaic impedance is represented in Fig. 13 with continuous line. Notice that the real part of the impedance extends from $R = \frac{V_T}{n\beta I}$ at high frequencies to $\frac{2V_T}{n\beta I}$ at low frequencies and the absolute value of the imaginary part has a

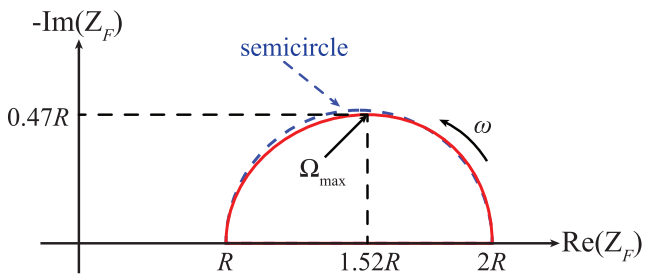

Figure 13. Nyquist plot of the faradaic impedance at large discharge currents and cathode widths (i.e. $L \gg \lambda$).

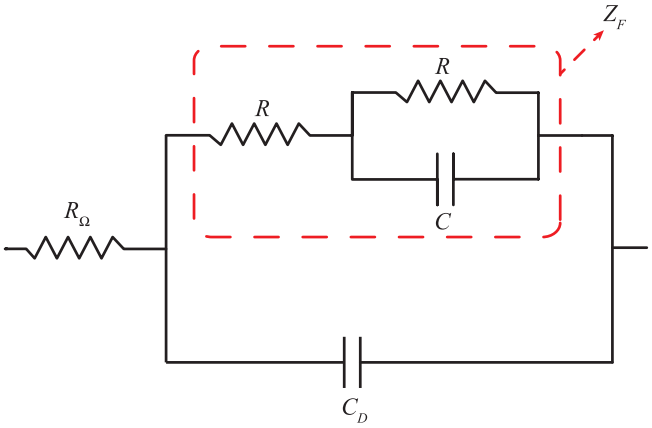

Figure 14. Approximate small-signal equivalent circuit of Li-air batteries operating at large discharge currents and with large cathode width ($L \gg \lambda$). The values of R_Ω, C_D, R, and C can be expressed in terms of physical parameters using eqs. 26, 27, 32, and 48, respectively. This circuit should be used with care in practical applications and instead one should use the more general circuit from Fig. 10.

maximum at $\Omega_{\max} = 0.647$, for which $\mathrm{Re}\left[Z_F\left(\Omega_{\max}\right)\right] = \frac{1.521 \times V_T}{n\beta I}$ and $\mathrm{Im}\left[Z_F\left(\Omega_{\max}\right)\right] = \frac{0.471 \times V_T}{n\beta I}$. At this maximum we can write

$$\frac{\omega_{max}\varepsilon\lambda^2}{D_{O_2,eff}} = \Omega_{\max} = 0.647 \qquad [45]$$

The impedance spectra represented in Fig. 13 can be approximated with a semicircle with radius equal to R and centered at $1.5 \times R$, where R is given by eq. 32 (see the dashed line in Fig. 13). It is known that such a semicircle can be modeled by a resistor R in series with another resistor of the same value R in parallel with a capacitor C (see the network encircled with dash line in Fig. 14). The impedance of this network is

$$Z_{F0} = R\left(1 + \frac{1}{1 + j\omega RC}\right) = R\left(1 + \frac{1}{1 + j\omega/\omega_{\max}}\right) \qquad [46]$$

where

$$\omega_{\max} = \frac{1}{RC} \qquad [47]$$

is the frequency at which the absolute value of the imaginary component of Z_{F0} is maximum. Eqs. 32, 45, and 47 can be solved to compute C as a function of the parameters of the battery

$$C = \frac{\varepsilon\lambda^2}{RD_{O_2,eff}\Omega_{\max}} = \frac{4A^2F^2\varepsilon n\beta D_{O_2,eff}C_O^{*2}}{V_T\Omega_{\max}I} \qquad [48]$$

where we have also used 19. Hence, small-signal equivalent circuit of Li-air batteries can be approximated with the one shown in Fig. 14 with R and C given by equations 32 and 48,where $\Omega_{\max} = 0.647$. The circuit represented in Fig. 14 and eq. 48 should be used with care in practical applications because it requires large discharge currents under which the porosity of the cathode can change significantly in time over the duration of the impedance measurements.

One can show that $\|Z_{F0}(\Omega) - Z(\Omega)\| < 4.3\%$ for all values of Ω. Hence, in the case of Li-air batteries with wide cathode width, we obtain an error less than 4.3% if we use the small-signal equivalent circuit shown in Fig. 14 instead of the complex circuit elements shown Fig. 10. Equations 32 and 48 are instrumental because they relate the small-signal circuit elements to the geometrical and electrochemical properties of the battery. By properly fitting the experimental data to the small-signal equivalent circuit shown in Fig. 14 one can extract information about the effective oxygen diffusion coefficient and the reaction rate constant.

Cells with narrow cathode widths and operating at small discharge/charge currents.— If both the cathode width and discharge current are small enough than

$$\frac{IL}{A} \ll 2FD_{O_2,eff}C_O^* \qquad [49]$$

and $L \ll \lambda$. Eq. 16 implies

$$\frac{V_T}{n\beta\eta_0}\ln\frac{kaL^2}{D_{O_2,eff}} \gg 1 \qquad [50]$$

where we have used the fact that $\eta_0 < 0$ because the battery is discharging. For standard Li-air batteries this condition implies that the absolute value of the overvoltage is of the same order or relatively small with respect to the thermal voltage, which implies that the reverse reaction current in the Butler-Volmer equation cannot be neglected. It can be shown that, when condition 50 is satisfied, model 5-11 predicts a real impedance, which slightly depends on the discharge current. However, in this case, it is worthless performing a quantitative comparison with experimental data because our results for the impedance spectra do not hold. Instead, one should use equations 25-29 for relatively large and medium discharge currents and cathode widths.

Conclusions

We have investigated the faradaic impedance of Li-air batteries and derived closed-form equations for the total electrochemical impedance in terms of the effective value of the diffusion coefficient of oxygen, specific cathode area, porosity, discharge current, reaction rate, oxygen concentration, and cathode width. It was shown that the relatively low effective diffusion coefficient of the oxygen in the cathode results in two slightly asymmetrical semicircles on the Nyquist diagram: one at low frequencies, where the oxygen diffusion dominates the operation of the cell and one at medium frequencies due to the combined effects of the double-layer capacitance and faradaic processes. Depending on the values of the effective diffusion coefficient, oxygen concentration, porosity, and cathode width the two semicircles can appear separately on the Nyquist plot, can merge into each other, or the effects at medium frequency can dominate. This model is valid for non-zero d.c. discharge currents and cannot be applied for zero d.c. currents, where the approximations made to derive it do not hold.

Using the analytical result for the spectral impedance we proposed a technique to obtain the effective diffusion coefficient of oxygen in the cathode and the reaction rate coefficient. This technique was tested on recent experimental data published by Adams et al.[31] for rechargeable organic Li-air batteries with different cathode structures. A very good agreement between our theoretical predictions and the published experimental results was obtained. The theory can predict quantitatively well the value of resistances on the Nyquist diagram for a large range of the oxygen concentration and discharge currents.

We have also developed a small-signal equivalent circuit for Li-air batteries and expressed the elements of the circuit in terms of the oxygen diffusion coefficient, oxygen concentration, discharge current, and other material and kinetic parameters, which make the model instrumental for extracting information about the material structure, reaction processes, and diffusion in the cathode. A high discharge current approximation is also presented for the small-signal equivalent circuit model. The approximate circuit contains only elementary components such as resistors and capacitors and can be implemented numerically easy in circuit simulators and used to fit the experimental data.

Appendix A

Dependence of Specific Area on the Structure of the Cathode

The microstructure of the cathode of Li-air batteries depends on the type of the material itself and on the fabrication process. Most often, the electron conductive material can be approximated as spheres with average radius $\bar{r}_{part}$ that touch each other in order

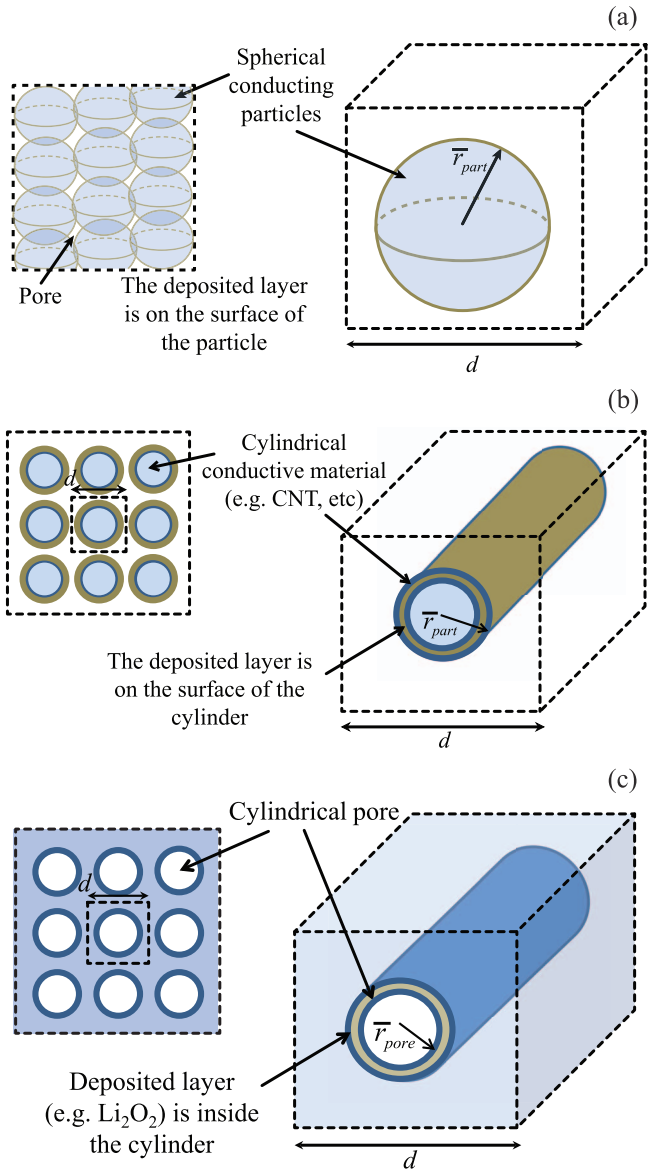

Figure A1. Possible approximations for the cathode structure in Li-air batteries: (a) the cathode is granulated, (b) the electron conductive material is cylindrical (such as in CNT networks), and (c) the pores are cylindrical (mostly used in theoretical models).

to conduct electric current.[33] In this case the reaction product deposits on the surface of the conductive spheres (see Fig. A1(a)) and the specific area is

$$a(\varepsilon) = \frac{3(1-\varepsilon)}{\bar{r}_{part}} \qquad [A1]$$

In other cases, for instance in the case of carbon nanotube networks (CNT) the electron conducting material can be approximated as cylinders with average radius $\bar{r}_{cyl}$ and the pores are the remaining space.[33,34] In this case the reaction product may deposit on the surface of the conductive cylinders like in Fig. A1(b), and the specific area can be found as

$$a(\varepsilon) = \frac{2(1-\varepsilon)}{\bar{r}_{cyl}} \qquad [A2]$$

In both cases, it is often convenient to approximate the pores of the cathode with cylindrical conduction channels with an initial average radius $\bar{r}_{pore}$ and porosity ε.[25] By inspecting Fig. A1(c) the specific area of the materials can be determined as

$$a(\varepsilon) = \frac{2\varepsilon}{\bar{r}_{pore}} \qquad [A3]$$

The specific area in real batteries is usually smaller than the values computed from A1-A3 because there exist regions on the cathode that are not accessible to the oxygen and those regions need to be eliminated.

Appendix B

Derivation of Eqs. 28-29

Variation of the oxygen concentration

Let $\tilde{c}_{O_2}(x)e^{j\omega t}$ be the variation in the oxygen concentration corresponding to a small-signal voltage perturbation $\tilde{\nu}e^{j\omega t}$. The variation of the oxygen concentration can be computed by expending eq. 5 in power series and keeping only the first-order terms

$$\varepsilon\frac{\partial[C_{O_2}(x)+\tilde{c}_{O_2}(x)e^{j\omega t}]}{\partial t} = D_{O_2,eff}\frac{d^2[C_{O_2}(x)+\tilde{c}_{O_2}(x)e^{j\omega t}]}{dx^2} - (U_\eta+\tilde{u}_\eta e^{j\omega t})[C_{O_2}(x)+\tilde{c}_{O_2}(x)e^{j\omega t}] \qquad [B1]$$

where $C_{O_2}(x)$ is the oxygen concentration at steady-state given by eq. 15 and

$$U_\eta = ka(\varepsilon)e^{-\frac{n\beta}{V_T}\eta_0} = \frac{D_{O_2,eff}}{\lambda^2} \qquad [B2]$$

$$\tilde{u}_\eta = -\frac{n\beta ka(\varepsilon)}{V_T}e^{-\frac{n\beta}{V_T}\eta_0}\tilde{\eta} \qquad [B3]$$

After linearizing B1, one obtains the following differential equation for the small-signal oxygen concentration

$$\frac{d^2\tilde{c}_{O_2}(x)}{dx^2} - \frac{1+j\Omega}{\lambda^2}\tilde{c}_{O_2}(x) - \frac{\tilde{u}_\eta C_{O_2}(x)}{D_{O_2,eff}} = 0 \qquad [B4]$$

where Ω is

$$\Omega = \frac{\omega\varepsilon\lambda^2}{D_{O_2,eff}} = \frac{\omega\varepsilon}{ka(\varepsilon)}e^{\frac{n\beta}{V_T}\eta_0} \qquad [B5]$$

and λ is given by 16. Eq. B4 is subject to the following boundary conditions

$$\left.\frac{d\tilde{c}_{O_2}(x)}{dx}\right|_{x=L} = 0 \qquad [B6]$$

$$\tilde{c}_{O_2}(x)\big|_{x=0} = 0 \qquad [B7]$$

which are obtained by linearizing 9 and 10. If we introduce notation

$$l = \frac{L}{\lambda} \qquad [B8]$$

and change the variable

$$y = \frac{x}{\lambda} \qquad [B9]$$

eqs. 15 and B4 lead to the following differential equation

$$\frac{d^2\tilde{c}_{O_2}(y)}{dy^2} - (1+j\Omega)\tilde{c}_{O_2}(y) = \frac{\tilde{u}_\eta C_O^*\lambda^2}{D_{O_2,eff}}(\cosh y - \tanh l\sinh y) \qquad [B10]$$

subject to

$$\left.\frac{dc(y)}{dy}\right|_{x=l} = 0 \qquad [B11]$$

$$c(y)|_{y=0} = 0 \qquad [B12]$$

The general solution of B10 is

$$\tilde{c}_{O_2}(y) = \frac{\tilde{u}_\eta C_O^*\lambda^2}{D_{O_2,eff}}\left(A\cosh\sqrt{1+j\Omega}y + B\sinh\sqrt{1+j\Omega}y - \frac{\cosh y - \tanh l\sinh y}{j\Omega}\right) \qquad [B13]$$

where A and B are two integration constants that can be found using boundary conditions B11 and B12. We obtain:

$$A = \frac{1}{j\Omega} \qquad [B14]$$

$$B = -\frac{\tanh\sqrt{1+j\Omega}l}{j\Omega} \qquad [B15]$$

which gives the following expression for the small-signal variation of the oxygen concentration

$$\tilde{c}_{O_2}(x) = \frac{\tilde{u}_\eta c_O^* \lambda^2}{D_{O_2,eff}} \frac{1}{j\Omega}\left[-\tanh\sqrt{1+j\Omega}l \sinh\frac{\sqrt{1+j\Omega}x}{\lambda} + \tanh l \sinh\frac{x}{\lambda} - \cosh\frac{x}{\lambda} + \cosh\frac{\sqrt{1+j\Omega}x}{\lambda}\right] \quad [B16]$$

Small-signal current

The small-signal current i can by computed by substituting 6 and 21-23 into 11

$$\tilde{i}e^{j\omega t} = \tilde{i}_F e^{j\omega t} + \tilde{i}_d e^{j\omega t} = 2AF\int_0^L [C_{O_2}(x) + \tilde{c}_{O_2}(x)e^{j\omega t}](U_\eta + u_\eta)dx + A\int_0^L C_d \frac{d}{dt}(\eta_0 + \tilde{\eta}e^{j\omega t})dx \quad [B17]$$

Expending B17 in power series and keeping only the first-order terms we obtain

$$\tilde{i} = \tilde{i}_F + \tilde{i}_d = 2AFU_\eta \int_0^L \tilde{c}_{O_2}(x)\,dx + 2AF\tilde{u}_\eta \int_0^L C_{O_2}(x)\,dx + j\omega C_D\tilde{\eta} \quad [B18]$$

where $\tilde{i}_F$ refers to the sum of the two integrals and $\tilde{i}_d$ to the last term in B17. $C_D = ALC_d$ is the total capacitance of the double layer. By substituting B16 and 15 into B18 and computing the integrals we obtain

$$\tilde{i}_F = \frac{2AF\tilde{u}_\eta C_O^* \lambda \tanh l}{1+j\Omega}\frac{1}{j\Omega}\left(\sqrt{1+j\Omega}\frac{\tanh\sqrt{1+j\Omega}l}{\tanh l} - 1\right) + 2AF\tilde{u}_\eta C_O^* \lambda \tanh l \frac{j\Omega}{1+j\Omega} \quad [B19]$$

Eq. 18 shows that $\frac{I\lambda}{2AFD_{O_2,eff}C_O^*} = \tanh l$ and together with eq. B2 results in

$$\frac{I}{U_\eta} = 2AF\lambda C_O^* \tanh l \quad [B20]$$

Substituting B20 into B19 we obtain

$$\tilde{i}_F = \frac{I}{U_\eta}\frac{\tilde{u}_\eta}{1+j\Omega}\left[\frac{1}{j\Omega}\left(\sqrt{1+j\Omega}\frac{\tanh\sqrt{1+j\Omega}l}{\tanh l} - 1\right) + j\Omega\right] \quad [B21]$$

Using eq. B3, the faradaic impedance can now be computed as

$$Z_F = -\frac{\tilde{\eta}}{\tilde{i}_F} = -\frac{\tilde{\eta}}{\tilde{u}_\eta}\frac{\tilde{u}_\eta}{\tilde{i}_F} = \frac{V_T}{n\beta ka(\varepsilon)} e^{\frac{n\beta}{V_T}\eta_0} \times \frac{\tilde{u}_\eta}{\tilde{i}_F} \quad [B22]$$

which leads to the following expression for Z_F

$$Z_F = \frac{V_T}{n\beta ka(\varepsilon)} e^{\frac{n\beta}{V_T}\eta_0} \times \frac{1}{\frac{I}{U_\eta}\frac{1}{1+j\Omega}\left[\frac{1}{j\Omega}\left(\sqrt{1+j\Omega}\frac{\tanh\sqrt{1+j\Omega}l}{\tanh l} - 1\right) + j\Omega\right]} \quad [B23]$$

By substituting B2 into B23 we obtain 28.

Appendix C

Mathematical Properties of Function F Defined in Eq. 28

Function $F(\Omega, l)$ has the following properties:

$$\lim_{l\to\infty} F(\Omega,l) = \frac{j\Omega(1+j\Omega)}{\sqrt{1+j\Omega}-1+(j\Omega)^2} = \frac{j\Omega}{\frac{(j\Omega)^2-1}{1+j\Omega}+\frac{1}{\sqrt{1+j\Omega}}} = \frac{j\Omega}{j\Omega-1+\frac{1}{\sqrt{1+j\Omega}}} \quad [C1]$$

$$\lim_{l\to 0} F(\Omega,l) = \lim_{l\to 0}\frac{j\Omega(1+j\Omega)}{1+j\Omega-1+(j\Omega)^2} = 1 \quad [C2]$$

$$\lim_{\Omega\to\infty} F(\Omega,l) = 1 \quad [C3]$$

$$\lim_{\Omega\to 0} F(\Omega,l) = \frac{1}{\frac{1}{2}+\frac{l}{\sinh 2l}} \in [1,2] \quad [C4]$$

$$\mathrm{Im}[F(\Omega,l)] \le 0 \quad [C5]$$

The Nyquist plot of function F is represented in Fig. C1 for different values of l. This impedance function displays a capacitive behavior at all frequencies (i.e. $\mathrm{Im}(F) < 0$) and become purely resistive when $\Omega \to 0$ or $\Omega \to \infty$.

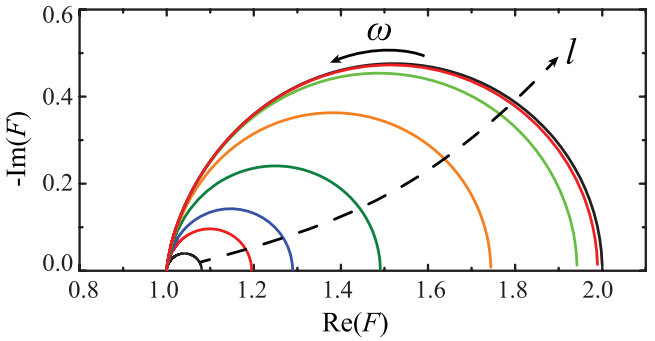

Figure C1. Nyquist plot of function F or different values of parameter l (starting from the smaller to the largest semicircle l = 0.5, 0.8, 1, 1.4, 2, 3, 4, and 10). Lower values of l corresponds to smaller discharge currents and narrow cathode widths; larger values of l corresponds to larger discharge currents and wider cathode widths.

List of Symbols

a	specific surface area of the porous material, cm^2/cm^3
A	cross-sectional of the cell, cm^2
$brugg$	Bruggeman constant
C_d	capacitance of the double-layer per unit area, F/cm^2
C_D	capacitance of the double-layer, F
c_{O_2}	oxygen concentration (depends on x and t), mol/cm^3
C_{O_2}	oxygen concentration at steady state (depends on x), mol/cm^3
C_O^*	initial oxygen concentration, mol/cm^3
$D_{O_2,eff}$	effective oxygen diffusion constant in the cathode, cm^2/s
D_{O_2}	diffusion constant of the oxygen in the electrolyte liquid, cm^2/s
F	Faraday's constant, 96,487 C/mol; also denotes function F defined in eq. 29
i	cell current, positive during discharge and negative during charge, A
i_F	faradaic component of the cell current, A
i_d	double-layer component of the cell current, A
I	cell current at steady-state, positive during discharge and negative during charge, A
I_F	faradaic component of the cell current at steady-state, A
I_d	double-layer component of the cell current at steady-state, A
k	reaction rate constant, cm/s
l	normalization cathode length (see eq. B8)
L	cathode length, cm
n	charge transfer coefficient
q	absolute value of electron charge, 1.6 × 10^{-19} C
$\bar{r}_{pore}$	average radius of the pores (cm)
R	resistance defined in eq. 32, Ω
R_Ω	combined resistance of the anode, separator, Li-ions, electrons, deposited layer, and contacts, Ω
r_C	reaction rate at the cathode, A/cm^3
t	time, s
T	temperature, 300 K
$\tilde{u}_\eta$	factor defined in eq. B3, s^{-1}
U_η	factor defined in eq. B2, s^{-1}
v	cell voltage, V
V	cell voltage at steady state, V
V_0	open cell voltage, V
V_T	thermal voltage ($V_T = \frac{RT}{F}$), V
Z	total impedance, Ω
Z_F	faradaic impedance, Ω

Greek Symbols

β	symmetry factor
ε	cathode porosity

λ	oxygen diffusion length as defined in 16, cm
η	overvoltage, V
η_0	overvoltage at steady-state, V
ω	angular frequency of a.c. perturbations (rad/s)
Ω	normalized angular frequency defined in eq. B5

A tilde "∼" symbol above a quantity denotes a small-signal (complex) variation

References

1. J. Read, *Journal of the Electrochemical Society*, **149**, A1190 (2002).
2. J. Read, K. Mutolo, M. Ervin, W. Behl, J. Wolfenstine, A. Driedger, and D. Foster, *Journal of the Electrochemical Society*, **150**, A1351 (2003).
3. J. Christensen, P. Albertus, R. S. Sanchez-Carrera, T. Lohmann, B. Kozinsky, R. Liedtke, J. Ahmed, and A. Kojic, *Journal of the Electrochemical Society*, **159**, R1 (2012).
4. J. P. Zheng, P. Andrei, M. Hendrickson, and E. J. Plichta, *Journal of the Electrochemical Society*, **158**, A43 (2011).
5. B. Kumar and J. Kumar, *Journal of the Electrochemical Society*, **157**, A611 (2010).
6. M. Mirzaeian, P. J. Hall, F. B. Sillars, I. Fletcher, M. M. Goldin, G. O. Shitta-bey, and H. F. Jirandehi, *Journal of the Electrochemical Society*, **160**, A25 (2013).
7. E. Barsoukov and J. R. Macdonald, *Impedance Spectroscopy: Theory, Experiment, and Applications*, Wiley (2005).
8. R. Mingant, J. Bernard, V. Sauvant-Moynot, A. Delaille, S. Mailley, J. L. Hognon, and F. Huet, in *Battery/Energy Technology*, N. Dudney, C. Johnson, and M. Yakovleva Editors, p. 41 (2011).
9. Z. F. Deng, Z. A. Zhang, Y. Q. Lai, J. Liu, J. Li, and Y. X. Liu, *Journal of the Electrochemical Society*, **160**, A553 (2013).
10. J. Xie, N. Imanishi, A. Hirano, Y. Takeda, O. Yamamoto, X. B. Zhao, and G. S. Cao, *Thin Solid Films*, **519**, 3373 (2011).
11. S. Yang, X. Wang, X. Yang, Y. Bai, Z. Liu, H. Shu, and Q. Wei, *Electrochimica Acta*, **66**, 88 (2012).
12. S. H. Jensen, A. Hauch, R. Knibbe, T. Jacobsen, and M. Mogensen, *Journal of the Electrochemical Society*, **160**, F244 (2013).
13. D. Malevich, B. R. Jayasankar, E. Halliop, J. G. Pharoah, B. A. Peppley, and K. Karan, *Journal of the Electrochemical Society*, **159**, F888 (2012).
14. F. Jaouen and G. Lindbergh, *Journal of the Electrochemical Society*, **150**, A1699 (2003).
15. F. Jaouen, G. Lindbergh, and K. Wiezell, *Journal of the Electrochemical Society*, **150**, A1711 (2003).
16. A. J. Bard and L. R. Faulkner, *Electrochemical Methods: Fundamentals and Applications*, Wiley (2000).
17. E. Levillain, A. Demortier, and J. P. Lelieur, *Journal of Electroanalytical Chemistry*, **394**, 103 (1995).
18. S. B. Adler, J. A. Lane, and B. C. H. Steele, *Journal of the Electrochemical Society*, **143**, 3554 (1996).
19. B. A. Boukamp, M. Verbraeken, D. H. A. Blank, and P. Holtappels, *Solid State Ionics*, **177**, 2539 (2006).
20. B. A. Boukamp and H. J. M. Bouwmeester, *Solid State Ionics*, **157**, 29 (2003).
21. P. Andrei, J. P. Zheng, M. Hendrickson, and E. J. Plichta, *Journal of the Electrochemical Society*, **157**, A1287 (2010).
22. P. Albertus, G. Girishkumar, B. McCloskey, R. S. Sanchez-Carrera, B. Kozinsky, J. Christensen, and A. C. Luntz, *Journal of the Electrochemical Society*, **158**, A343 (2011).
23. P. Andrei, J. P. Zheng, M. Hendrickson, and E. J. Plichta, *Journal of the Electrochemical Society*, **159**, A1 (2012).
24. X. Li and A. Faghri, *Journal of the Electrochemical Society*, **159**, A1747 (2012).
25. S. S. Sandhu, J. P. Fellner, and G. W. Brutchen, *Journal of Power Sources*, **164**, 365 (2007).
26. V. Viswanathan, K. S. Thygesen, J. S. Hummelshoj, J. K. Norskov, G. Girishkumar, B. D. McCloskey, and A. C. Luntz, *The Journal of Chemical Physics*, **135**, 214704 (2011).
27. J. Z. Chen, J. S. Hummelshoj, K. S. Thygesen, J. S. G. Myrdal, J. K. Norskov, and T. Vegge, *Catal Today*, **165**, 2 (2011).
28. I. J. Ong and J. Newman, *Journal of the Electrochemical Society*, **146**, 4360 (1999).
29. M. Doyle, J. P. Meyers, and J. Newman, *Journal of the Electrochemical Society*, **147**, 99 (2000).
30. D. H. J. Baert and A. A. K. Vervaet, in *Telecommunications Energy Conference, 2003. INTELEC '03. The 25th International*, p. 733 (2003).
31. J. Adams, M. Karulkar, and V. Anandan, *Journal of Power Sources*, **239**, 132 (2013).
32. L. Wang, X. Zhao, Y. Lu, M. Xu, D. Zhang, R. S. Ruoff, K. J. Stevenson, and J. B. Goodenough, *Journal of the Electrochemical Society*, **158**, A1379 (2011).
33. Y. Wang, *Electrochimica Acta*, **75**, 239 (2012).
34. G. Q. Zhang, J. P. Zheng, R. Liang, C. Zhang, B. Wang, M. Au, M. Hendrickson, and E. J. Plichta, *Journal of the Electrochemical Society*, **158**, A822 (2011).
35. X.-Z. Wu, T. Morikawa, K. Uchiyama, and T. Hobo, *The Journal of Physical Chemistry B*, **101**, 1520 (1997).